The Astrophysical Journal, 912:54 (10pp), 2021 May 1 https://doi.org/10.3847/1538-4357/abe87b

Multiwavelength and Neutrino Emission from Blazar PKS 1502+106

Xavier Rodrigues, Simone Garrappa, Shan Gao, Vaidehi S. Paliya, Anna Franckowiak, and Walter Winter
Deutsches Elektronen-Synchrotron DESY, D-15738 Zeuthen, Germany; xavier.rodrigues@desy.de
Received 2020 September 10; revised 2021 February 15; accepted 2021 February 19; published 2021 May 4

Abstract

In 2019 July, the IceCube experiment detected a high-energy neutrino from the direction of the powerful blazar PKS 1502+106. We perform multiwavelength and multimessenger modeling of this source, using a fully selfconsistent one-zone model that includes the contribution of external radiation fields typical of flat-spectrum radio quasars. We identify three different activity states of the blazar: one quiescent state and two flaring states with hard and soft gamma-ray spectra. We find two hadronic models that can describe the multiwavelength emission during all three states: a leptohadronic model with a contribution from photohadronic processes to X-rays and gamma-rays, and a proton synchrotron model, where the emission from keV to 10 GeV comes from proton synchrotron radiation. Both models predict a substantial neutrino flux that is correlated with the gamma-ray and soft X-ray fluxes. Our results are compatible with the detection of a neutrino during the quiescent state, based on event rate statistics. We conclude that the soft X-ray spectra observed during bright flares strongly suggest a hadronic contribution, which can be interpreted as additional evidence for cosmic-ray acceleration in the source independently of neutrino observations. We find that more arguments can be made in favor of the leptohadronic model vis-a-vis the proton synchrotron scenario, such as a lower energetic demand during the quiescent state. However, the same leptohadronic model would be disfavored for flaring states of PKS 1502+106 if no IceCube events were found from the direction of the source before 2010, which would require an archival search.

Unified Astronomy Thesaurus concepts: Blazars (164); Cosmological neutrinos (338); Astronomy data modeling (1859); Gamma-ray sources (633); Ultra-high-energy cosmic radiation (1733); High-luminosity active galactic nuclei (2034); Astronomical simulations (1857)

1. Introduction

High-energy neutrinos are a unique probe of the high-energy universe capable to identify the acceleration regions of cosmic rays (for recent reviews, see Gallo Rosso et al. 2018; Vitagliano et al. 2019). A first milestone was the detection of a diffuse neutrino flux with the IceCube neutrino observatory in 2013 (Aartsen et al. 2013). However, the origin of those neutrinos is still unknown. Active Galactic Nuclei (AGN) are considered promising candidate sources (e.g., Stecker et al. 1991; Mannheim et al. 1992; Mannheim 1993, 1995; Szabo & Protheroe 1994; Mastichiadis 1996; Protheroe 1999; Atoyan & Dermer 2001; Becker 2008; Dimitrakoudis et al. 2012; Becker Tjus et al. 2014; Murase 2017). In particular their relativistic jets are promising sites of cosmic-ray acceleration, which could produce neutrinos in interactions with ambient photon fields or matter in or close to the source.

To identify possible sources, IceCube has set up a target of opportunity program, which allows for the rapid search of multiwavelength counterparts to high-energy neutrino track events (Aartsen et al. 2017). Thanks to this program, the gamma-ray blazar TXS 0506+056 could be identified as a first compelling neutrino source at the 3σ level: the high-energy neutrino event IceCube-170922A was found in spatial coincidence with the blazar position and in temporal coincidence with a significant flare in gamma-rays (Aartsen et al. 2018a). An additional excess of lower-energy neutrinos arriving within a 160 day time window in 2014/15 was identified at the 3.5σ confidence level in an archival search for a time-dependent neutrinos signal from the direction of TXS 0506+056 (Aartsen et al. 2018b). However, this neutrino excess was not accompanied by a gamma-ray flare (Garrappa et al. 2019).

Other possible neutrino blazar associations at lower significance have been pointed out by e.g., Franckowiak et al. (2020), Giommi et al. (2020), Garrappa et al. (2019), Krauß et al. (2018), Kadler et al. (2016). Of particular interest is the spatial coincidence of IceCube-190730A with PKS 1502+106, which is the 15th brightest gamma-ray source at >100 MeV in terms of energy flux among 2863 sources in the fourth catalog of AGN detected by Fermi-LAT (4LAC; Ajello et al. 2019). Given the large redshift of 1.84 (Hewett & Wild 2010) the source must have an extremely high intrinsic luminosity. It is also highly variable in the gamma-ray band (see e.g., Abdo et al. 2010). While the source did not show an excess in gamma-rays during the arrival of IceCube-190730A, the radio flux shows a long-term outburst starting in 2014 and reaching the highest flux density ever reported from this source during the arrival of IC-190730A (Kiehlmann et al. 2019; Franckowiak et al. 2020), which may indicate a long-term activity of the central engine. IceCube-190730 has an estimated neutrino energy of 300 TeV and a 67% signalness[1] based on the procedure by Blaufuss et al. (2020).

PKS 1502+106 is a broad emission line quasar first identified as a strong radio source in the 178 MHz pencil beam survey (Crowther & Clarke 1966). At radio frequencies, the source is highly variable and observations from very long baseline interferometry have revealed a core-dominated, one-sided, curved radio jet (e.g., An et al. 2004). PKS 1502+106 has exhibited large-amplitude optical variability (>2.5 mag; Morton et al. 2008) and the detection of a high degree of optical polarization (up to ∼20%) suggests the dominance of the synchrotron emission at these wavelengths. Shen et al. (2011) studied the optical spectrum of this object

[1] https://gcn.gsfc.nasa.gov/notices_amon_g_b/132910_57145925.amon

taken with the Sloan Digital Sky Survey and reported a central black hole mass of $10^{9.64\pm0.44}M_{\odot}$. In the high-energy gamma-ray band, PKS 1502+106 was not detected with the Energetic Gamma-Ray Experiment Telescope (EGRET; Hartman et al. 1999). However, a significant >100 MeV radiation was detected within the first few months of Fermi-LAT operation when the blazar was undergoing a huge γ-ray outburst (Abdo et al. 2010). Since then, PKS 1502+106 has been extensively studied across the electromagnetic spectrum (see Pian et al. 2011; Karamanavis et al. 2016; Paliya et al. 2017; Ding et al. 2019; Shao et al. 2019).

In this work we describe the multiwavelength emission from PKS 1502+106 and its possibly associated neutrino emission. While earlier models frequently assume that the gamma-rays are produced by neutral pion decays accompanying the neutrino production (Kadler et al. 2016), the observation of neutrinos from TXS 0506 + 056 has taught us that observational constraints in the X-ray band can limit the hadronic contribution. In that case, the neutrino flux has been shown to be explained by a hybrid leptohadronic model (e.g., Gao et al. 2018; Keivani et al. 2018; Oikonomou et al. 2019). We apply this model to PKS 1502+106 where the neutrino-producing hadronic processes only contribute to X-ray and possibly TeV gamma-rays, where the rest of the multiwavelength spectrum is produced leptonically. We also examine another possibility, where the GeV gamma-rays are explained by proton synchrotron emission (see e.g., Diltz et al. 2015; Cerruti et al. 2019). Since PKS 1502+106 falls in the blazar subclass of flat-spectrum radio quasars (FSRQs), the GeV emission can originate from inverse-Compton scattering of radiation fields external to the jet (Rodrigues et al. 2019). This effect is included in the models explored in this work.

2. Methods

In this section, we first explain the process for identifying the different relevant epochs in terms of gamma-ray emission. We then describe the radiation model, including the treatment of external radiation fields. Finally, we discuss the methods used to search the parameter space of the source.

2.1. Analysis of the Multiwavelength Behavior

The majority of the observed gamma-ray blazars exhibit a highly variable behavior on timescales from minutes to years (Meyer et al. 2019). Measurements of these characteristic timescales and the spectral properties of the sources during these bright flaring states can provide useful insights about the emission region and the mechanisms behind the production of the observed gamma-rays.

We define a simple method to distinguish flaring states from the quiescent state of the source. To that end we utilize the gamma-ray lightcurve for 11 yr of observation of PKS 1502 +106 provided by Franckowiak et al. (2020), as shown in the top panel of Figure 1 and the corresponding Fermi-LAT spectral indices are shown in the bottom panel. While there is no standard method to define a quiescent state in a blazar lightcurve, we consider the average of the measured fluxes in the low-activity period from 2010 February to 2014 December weighted by the time duration of each bin as a proxy for the quiescent state. In order to identify the brightest flaring periods for the source, we use the Bayesian blocks representation of the lightcurve (Scargle et al. 2013) and we define all the Bayesian blocks with a flux level higher than the calculated average as flaring states of the source.

We define three different multiwavelength states for PKS 1502+106 based on the gamma-ray data, comparing the average index in each Bayesian Block with the average index and error from the quiescent proxy: (i) a quiescent state, with low gamma-ray flux , (ii) a gamma-ray flaring state with hard spectral index compared to the average observed value of $\bar{\Gamma} = (2.39 \pm 0.13)$ (hard flares) and (iii) a gamma-ray flaring state with spectral index compatible to the one observed during the quiescent proxy period, within the average uncertainty band (soft flares).

In general, we find a good correlation between the gamma-ray and optical fluxes in Franckowiak et al. (2020). The X-ray sampling is poor and the variability observed in radio surveys is slow, so observations in these bands are not suitable for further refining the definition of the different states.

The three activity states are highlighted in different colors in Figure 1. The 11 yr period is characterized by a quiescent state, with a total duration of about 3.8 yr (blue shaded areas). The detection of IceCube-190730A falls into this state, as indicated by the dashed red line. The total duration of the other states are 3.7 yr for the hard flaring state and 3.5 yr for the soft flaring state, highlighted in Figure 1 with yellow and pink shaded areas, respectively.

In Table 1 we report the three observation periods that will be used to represent each of the three activity states of the source later in this work, when the numerical radiation models are used to describe the multiwavelength emission. These simultaneous multiwavelength data sets were adopted from Franckowiak et al. (2020).

2.2. Numerical Radiation Model

For each of the three states, we numerically model the multiwavelength and neutrino emission of PKS 1502+106 using the time-dependent simulation code AM^3 (Gao et al. 2017), which solves the system of coupled differential equations describing the transport of all relevant particles interacting in the blazar jet. Nonthermal electrons and protons are assumed to be accelerated and subsequently injected into a single radiative zone in the jet. This zone is modeled as a blob that is spherical in its comoving frame and spatially homogeneous. Although there may be multiple emitting regions in the jet of PKS 1502+106, in the models explored here this single zone is responsible for the multiwavelength emission between the optical and the gamma-ray regimes, as well as neutrino production.

The comoving radius of the blob is denoted as $R'_{\rm b}$ (quantities in the blob's comoving frame are primed). We assume the magnetic field is randomly oriented within the blob with a homogeneous strength B'. The blob is moving at relativistic speed relative to the supermassive black hole with a Lorentz factor of $\Gamma_{\rm b}$ and we assume the jet is observed at an angle $\theta_{\rm obs} = 1/\Gamma_{\rm b}$ relative to its axis, resulting in a Doppler factor of $\delta_D = \Gamma_{\rm b}$. The distance of the blob to the supermassive black hole is parameterized by the dissipation radius, $R_{\rm diss}$, and its impact on the model is discussed in Section 2.3.

Electrons are assumed to be accelerated to a simple power-law distribution, $dN_e/d\gamma_e \propto \gamma^{-p_e}$, from a minimum to a maximum Lorentz factor, $\gamma_e^{\rm min}$ and $\gamma_e^{\rm max}$. For protons we also test whether the observations can be better explained with a break on the spectrum at a Lorentz factor

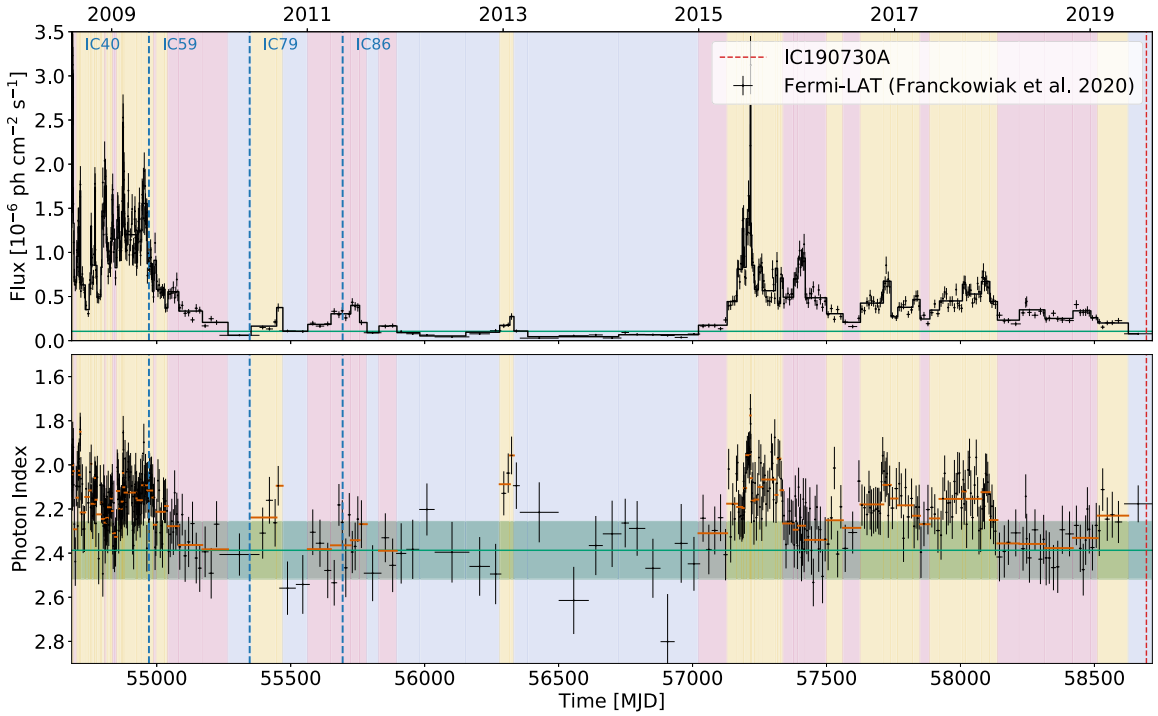

Figure 1. Top: eleven-year Fermi-LAT lightcurve of PKS 1502+106 (Franckowiak et al. 2020), divided for the purposes of this analysis into three characteristic states: quiescent (blue), flaring with a hard gamma-ray spectrum (hard flares, yellow) and flaring with a soft gamma-ray spectrum (soft flares, pink). The green line shows the average flux of 3×10^{-7} ph cm^{-2} s^{-1}. Bottom: Fermi-LAT spectral index across the same 11 yr time period. The green line shows the average spectral index ($\bar{\Gamma} = 2.31$), from where we draw the distinction between hard ($\Gamma < \bar{\Gamma}$) and soft ($\Gamma > \bar{\Gamma}$) flares, and the green band is its respective 1σ uncertainty. The red lines show the average spectral index in the time window of each flare.

Table 1
Information about the Three Activity States of PKS 1502+106 Identified in Figure 1

State	Total Duration [yr]	Representative Data Set
Quiescent	3.8	MJD 58664-58724
Hard Flare	3.7	MJD 57210-57219
Soft Flare	3.5	MJD 58107-58125

Note. The representative data sets refer to multiwavelength observations from each of the three activity states, which are used in this work to constrain the source models. The quiescent state observations are coincident with the neutrino detection. The three data sets were compiled by Franckowiak et al. (2020): the quiescent state data can be found in the bottom right panel of Figure 4 of that work, and the data from the two flaring states in the bottom right panel of the same figure.

$\gamma_p^{\rm min} < \gamma_p^{\rm break} < \gamma_p^{\rm max}$, where the spectral index changes from $p_p^{\rm low}$ to $p_p^{\rm high} > p_p^{\rm low}$. The normalization of these acceleration spectra is quantified by means of the total (energy-integrated) luminosity deposited into nonthermal electrons, L'_e, and protons, L'_p.

2.3. External Radiation Fields

Being an FSRQ, PKS 1502+106 possesses a broad line region (BLR) surrounding the accretion disk, which reprocesses and partially isotropizes the emission from the powerful accretion disk surrounding the black hole. The emission from the disk can be observed as a thermal bump in the optical/ultraviolet (UV) regime ($\sim$5 eV) during the quiescent state of the blazar (Franckowiak et al. 2020), see also Section 3. The observed UV flux translates to a luminosity of $L_{\rm disk} = 5 \times 10^{46}$ erg s^{-1}. This value is roughly consistent with that obtained by Shen et al. (2011) using broad Mg II and C IV emission line luminosities, assuming the scaling factors proposed by Francis et al. (1991).

We assume the BLR to be a thin shell located at a radius of $R_{\rm BLR} = 10^{17}$ cm around the supermassive black hole. Although lower compared to the general trend noted by Ghisellini & Tavecchio (2009), it is within the statistical uncertainties given by the spread of values found in the overall AGN population. We further assume that the BLR reprocesses about 10% of the power output by the accretion disk (Greene & Ho 2005), re-emitting it isotropically in the rest frame of the black hole.[2] Inside the volume surrounded by the BLR, the energy density of this isotropic field is constant and proportional to $L_{\rm disk} R_{\rm BLR}^{-2}$. In the rest frame of the jet, this energy density receives a relativistic boost given by $\Gamma_{\rm b}^2$, and the photon frequencies are Doppler-shifted by a factor $\Gamma_{\rm b}$.

Outside the BLR, the energy density of the external fields declines with distance to the black hole according to Equations (19) and (20) from Ghisellini & Tavecchio (2009). Therefore, in the case where the blob lies outside the BLR ($R_{\rm diss} > R_{\rm BLR}$), the energy density of the external fields seen by the particles in the blob depends inversely on the dissipation radius $R_{\rm diss}$. Furthermore, the frequency of the disk photons as seen in the rest frame of the jet also decreases with the dissipation radius

[2] Most of the disk radiation processed by the BLR is in fact re-emitted as atomic lines and not a thermal continuum (Greene & Ho 2005). However, the results of this study are not affected by this distinction, since most of the atomic emission will lie on a similar frequency range as the thermal disk emission (the Lyα line has an energy of 10 eV for hydrogen).

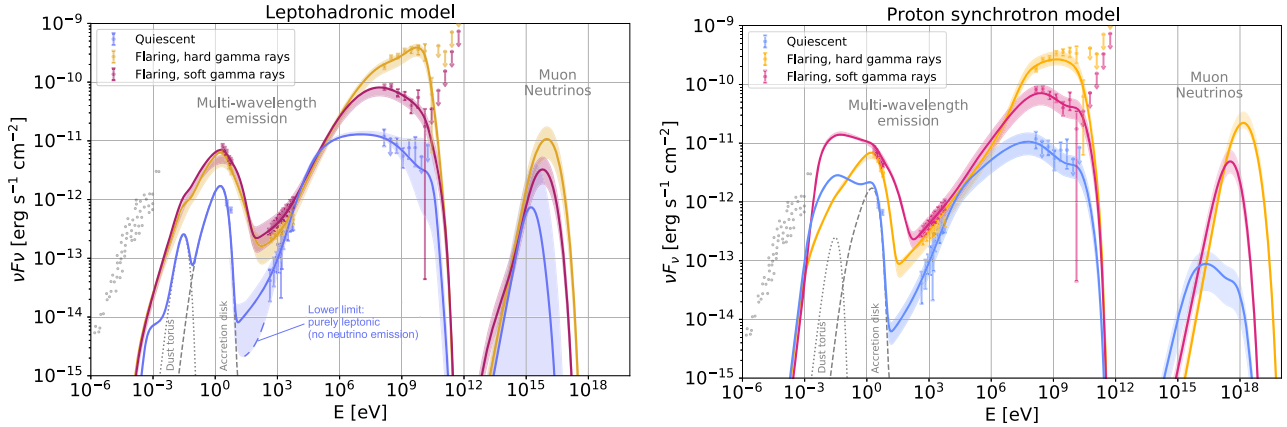

Figure 2. The colored curves show the predicted multiwavelength fluxes and all-flavor neutrino spectra from PKS 1502+106 obtained with the leptohadronic model (left) and the proton synchrotron model (right) under three different parameter sets, indicated in Table 2. The shaded areas correspond to the uncertainty in the nonthermal proton power, also indicated in Table 2. The colored data points represent multiwavelength flux observations during each of the three states (see Figure 1 and Table 1). The gray points show archival radio data from the source. The interaction zone responsible for the optical/UV, X-ray, gamma-ray and neutrino emission is too compact to produce this radio emission (due to strong synchrotron self-absorption). The radio flux must therefore originate in the synchrotron emission from a larger region of the jet, and is therefore not directly predicted by our one-zone model.

for values of $R_{\rm diss} > R_{\rm BLR}$, following the angular dependence of the Doppler factor.[3]

Additionally to the disk radiation reprocessed by the BLR, we also consider thermal infrared emission from a dusty torus surrounding the disk. However, because of the larger volume spanned by this emission, the corresponding photon energy density is negligible compared to the BLR emission in all the cases considered. The inclusion of a subdominant component up to X-rays from the black hole corona would also not affect the results in any of the cases modeled.

2.4. Parameter Search

We have searched the parameter space of the source in two distinct regimes, distinguished primarily by the strength of the magnetic field in the jet: in the *leptohadronic model* we admit values of $B' \leqslant 1$ G, while in the *proton synchroton model* these values are higher, $B' \geqslant 10$ G. In this regime, the proton synchrotron emission can contribute to the observed high-energy fluxes, while in the leptohadronic model protons will only contribute significantly through photohadronic interactions.

The parameter space was scanned using a genetic algorithm similar to that used by Rodrigues et al. (2019), with the purpose of minimizing the χ^2 value of the predicted multiwavelength fluxes compared to data. Additionally to using an efficient search algorithm, the method also involves the simulation of a large number of parameter sets, in the order of 10^6 for each activity state.

3. Results

Using the numerical models described in the previous section, we have calculated the multiwavelength and neutrino spectra for PKS 1502+106 during the different epochs. We have then compared the neutrino results to the statistical expectations based on the IceCube sensitivity.

[3] As a good approximation, we consider the photons impinging on the blob from the direction tangential to the BLR, at an angle $\xi = \arcsin(R_{\rm BLR}/R_{\rm diss})$ away from the jet axis. The Doppler factor of the BLR photons in the rest frame of the jet is then given by $\delta = \Gamma_{\rm b}(1 - \beta\cos\xi)$, where $\beta = \sqrt{(1 - 1/\Gamma_{\rm b}^2)}$.

3.1. Multimessenger Emission

The emitted fluxes during the three activity states of PKS 1502+106 are shown in Figure 2, as predicted by the leptohadronic and the proton synchrotron models (left and right panels, respectively). The fluxes shown as colored data points correspond to three well-covered multiwavelength observations analyzed in Franckowiak et al. (2020) that are representative of the different states considered for the source in this work: in blue we represent observations during the quiescent state, in yellow during hard flares, and in pink for soft flares. The data points shown in the figure were the ones used to fit the model in each of the three epochs. The gray points in the radio band correspond to historical radio data. The neutrino-emitting region in the jet (i.e., the blob) is necessarily too compact to explain the archival radio observations from the source. This is because the high radiation density necessary for hadronic processes leads to efficient synchrotron self-absorption at low frequencies, which limits the outgoing radio flux. Therefore, we assume that the radio observations originate from electrons radiating in a more extended region of the jet.

Both the multiwavelength and neutrino fluxes have a best-fit result, represented by the colored curves, and an uncertainty band. The best-fit parameters are listed in Table 2. The uncertainty band is obtained by varying the power in accelerated protons (while keeping all other parameters constant) until the flux (in either X-rays or gamma-rays) deviates from the best-fit model by $\pm 40\%$. This variation corresponds roughly to the 1σ spread we find in the individual flux bins throughout each of the three activity states. This band is intended to reflect the variability of the high-energy emission observed in the duration of a given activity state, which cannot be fully represented by a single set of simultaneous data. This variability in the data leads to an uncertainty in the neutrino flux emitted by the source throughout each of the three states, which is not necessarily constant; the uncertainty bands allow us to assess this uncertainty when evaluating the predicted number of events in IceCube. At the same time, we require the models to describe well the simultaneous multiwavelength data that is available (namely the three data sets shown in Figure 2). We therefore use these three data sets to test the goodness of fit

Table 2
Parameter Values Underlying the Results of the Leptohadronic and Proton Synchrotron Models, for Each of the States Identified in Figure 1

Model	Leptohadronic			Proton Synchrotron		
State	Quiescent	Hard Flare	Soft Flare	Quiescent	Hard Flare	Soft Flare
$R'_{\rm b}$ [cm, log]	16.0	15.9	15.9	16.0	16.0	16.0
B' [G]	0.3	0.3	0.6	10.0	12.6	15.8
Bulk Lorentz factor $\Gamma_{\rm b}$	27.6	28.7	26.2	40.0	49.2	42.6
$R_{\rm diss}/R_{\rm BLR}$	1.3	1.3	1.6	$\geqslant$2.5	$\geqslant$2.5	$\geqslant$2.5
L'_e [erg s^{-1}, log]	43.5	44.6	44.2	42.0	41.6	42.6
L'_p [erg s^{-1}, log]	$\leqslant 44.8^{+0.8}$	$45.6^{+0.2}_{-0.2}$	$46.0^{+0.2}_{-0.1}$	$45.5^{+0.4}_{-0.3}$	$45.3^{+0.0}_{-0.2}$	$45.1^{+0.1}_{-0.2}$
$\gamma_e'^{\rm min}$, log	1.0	3.8	3.3	2.0	3.0	1.9
$\gamma_e'^{\rm max}$, log	3.7	4.5	4.2	3.0	3.1	3.5
p_e	2.1	3.6	1.2	2.1	3.5	2.1
$\gamma_p'^{\rm min}$, log	5.4	5.2	4.6	2.0	8.1	6.8
$\gamma_p'^{\rm break}$, log	…	…	…	6.7	…	…
$\gamma_p'^{\rm max}$, log	6.1	7.1	6.9	8.5	9.2	8.3
$p_p^{\rm low}$	…	…	…	0.3	…	…
$p_p^{\rm high}$	1.5	1.5	1.5	2.3	2.4	1.5
$\chi^2_{\rm SED}$/d.o.f.	0.3	2.7	1.0	0.7	3.8	1.6
$N_{\rm events}$ per year	$0.47^{+2.19}_{-0.47}$	$3.19^{+1.90}_{-1.71}$	$1.27^{+0.8}_{-0.55}$	$0.02^{+0.01}_{-0.01}$	$0.05^{+0.02}_{-0.01}$	$0.05^{+0.02}_{-0.02}$
$N_{\rm events}$ (total)	$1.77^{+8.23}_{-1.77}$	$10.94^{+6.56}_{-5.84}$	$4.32^{+2.71}_{-1.87}$	$0.07^{+0.05}_{-0.04}$	$0.17^{+0.06}_{-0.03}$	$0.17^{+0.06}_{-0.04}$

Note. Primed quantities refer to the rest frame of the jet. The ranges in the values of the proton luminosity correspond to the uncertainties of the model, resulting in the shaded regions in Figure 2. We also report the reduced χ^2 values for the multiwavelength SEDs predicted by each model, describing the goodness of fit. In the two bottom rows, we list the predicted number of neutrino events per year in IceCube, as well as the total expected number of events integrated over the eleven-year period. The yearly rates correspond to the IC86 configuration of the IceCube detector, since they were calculated using the effective area of that configuration. For the total number of events, we take into account the different detector configurations over the years, as depicted by the dashed vertical lines in Figure 1.

of the models, which are reported in Table 2 in the form of a χ^2 value per degree of freedom.

In both models, the observed UV fluxes result from the electron synchrotron emission during the flaring states, and from an exposed accretion disk during the quiescent state. The differences between the models impact primarily the high-energy emission: in the right-hand panel of Figure 2, proton synchrotron dominates the emitted gamma-ray flux below 1 GeV and, in the quiescent state, also the X-rays. As we can see in Table 2, the minimum proton Lorentz factor required in this model can reach values up to $\gamma_p^{\rm min} \sim 10^8$, which is necessary to ensure that the proton synchrotron emission is not significantly below X-ray frequencies.

On the contrary, in the leptohadronic model (left panel), the gamma-ray emission is mostly dominated by external Compton scattering. This is possible due to the location of the blob in the vicinity of the BLR perimeter ($R_{\rm diss} \gtrsim R_{\rm BLR}$, as listed in Table 2), while in the proton synchrotron model the blob lies far outside the BLR and thus external fields do not play a significant role. On the other hand, the photons from hadronic processes explain the X-ray observations, especially during the flaring states. As detailed in the next section, in both models the predicted location of the gamma-ray emission is consistent with current constraints from Fermi-LAT observations of the source (Abdo et al. 2010). On the contrary, radio knots are typically observed further from the central engine, where the jet eventually becomes optically thin to radio emission (Karamanavis et al. 2016).

As we can see by the blue band in the left-hand panel of Figure 2, the quiescent state can fit within a range of proton-injection luminosities, which leads to different levels of neutrino emission. The best fit, represented by the blue curves, has a hadronic component, which is responsible for the neutrino emission. When this hadronic component is completely removed, we obtain the lower limit of the blue band, and there is no neutrino emission (the blue neutrino band extends down to zero). In this purely leptonic limit, the simultaneous data shown in blue is not fit as well in X-rays and gamma-rays above 1 GeV. However, as mentioned earlier, all results within the colored bands lie within the 1σ spread in the fluxes observed during the quiescent state in the 11 yr lightcurve. Therefore, the quiescent state of the source is in general compatible with a purely leptonic scenario.

Contrary to the quiescent state, our parameter search has revealed that the flaring states are not easily explained by a purely leptonic scenario. The relatively bright and soft X-ray spectrum (see pink and yellow data points) must harden around MeV energies in order to explain the high gamma-ray fluxes, especially during the hard gamma-ray flares. As explained in detail below, in both the proton synchrotron and leptohadronic models these X-rays originate in cascades initiated by high-energy hadronic photons, which provide a necessary component to bridge the two humps of the emission spectrum.

In order to help understand the details of the two models, in Figure 3 we break down the multiwavelength fluxes shown in Figure 2 into their different radiative components. In the three left panels, we show the processes responsible for the emission in the leptohadronic model. As mentioned earlier, gamma-ray fluxes are dominated by Compton scattering (light blue curve) of the external thermal fields. Additionally, the accelerated protons emit photons through photopion production (yellow) and Bethe–Heitler pairs, which in turn radiate through synchrotron and inverse Compton (orange). When these high-

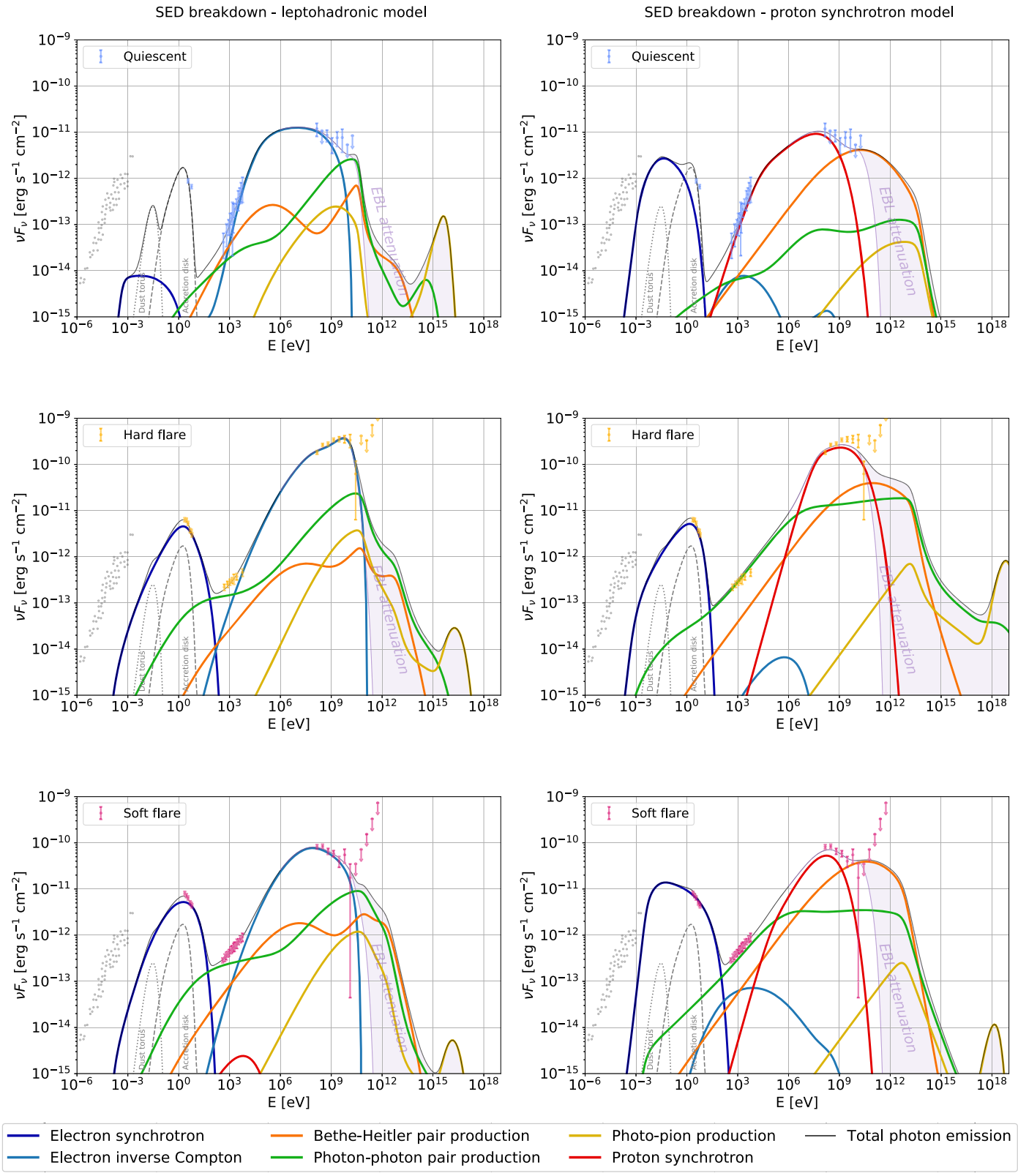

Figure 3. Breakdown of the spectrum during the different states into the different radiative processes for the leptohadronic model (left) and the proton synchrotron model (right).

energy photons annihilate with lower-energy target photons, an electromagnetic cascade is created in the jet, whose emission is shown in green. Above 100 GeV, the emitted radiation is strongly attenuated by EBL interactions, as represented by the purple band.

Considering only the leptonic emission, we would have necessarily a deep gap between UV and X-rays, and the inverse Compton emission provides a hard spectrum between X-rays and gamma-rays. In the quiescent state (upper left panel), this hard inverse Compton spectrum can explain the X-ray

observations above 1 keV, while the photons from cascades and the Bethe–Heitler emission contribute to the soft X-rays. On the contrary, in the flaring states (middle and lower panels), the observed X-ray flux is softer. The cascade emission is therefore necessary in this model to explain observations in this energy range. This seems to provide some evidence of proton interactions in the source solely from the perspective of the multiwavelength behavior of the source.

Additionally to X-rays, the cascades from hadronic photons also contribute significantly to the gamma-ray flux above 1 GeV in the quiescent state. As shown previously in Figure 2, when the hadronic component is removed completely, the two Fermi-LAT data points at the highest energies are not explained, leading to a worse fit. On the other hand, gamma-rays below 1 GeV are independent of this hadronic contribution.

In the right panels of Figure 3 we show a breakdown of the emission in the proton synchrotron model. In the quiescent state the X-ray fluxes are explained by the proton synchrotron emission, as well as gamma-rays up to 100 MeV. Above this energy, the spectrum is dominated by the emission from Bethe–Heitler pairs. In the flaring states, when the observed X-ray spectrum is softer, it is the cascade emission that dominates that energy range, such as in the leptohadronic model.

Regarding the neutrino emission, the proton synchrotron model predicts a high peak energy of around 10 PeV to 1 EeV, while in the leptohadronic model the neutrinos peak around 1–10 PeV. The neutrino energies are determined by the maximum proton energy, which is constrained by observations in both models. In the proton synchrotron model, it is constrained by gamma-ray observations, since these are explained by the proton synchrotron emission. In the leptonic model, the maximum protons energy is constrained mainly by the X-ray fluxes, since the extent of the electromagnetic cascade depends on the energy of the interacting protons.

Importantly, the leptohadronic model predicts a quiescent-state neutrino flux a factor 10 higher compared to proton synchrotron. This is due to the high density of radiation from the accretion disk whose energy is boosted in the jet rest frame up to the photopion production threshold. In the proton synchrotron model, on the other hand, the main target for photopion production are nonthermal photons. During the flaring states, there is a high density of UV photons from electron synchrotron, thus enhancing the neutrino emission. During the quiescent state, this nonthermal emission is dim, and the neutrino production is therefore low. The sharp dip in the photon spectrum between the cutoff of the electron synchrotron and the onset of the proton synchrotron leads to a double hump in the neutrino spectrum that can be seen in Figure 2. In the leptohadronic model there are no such structures in the neutrino spectrum because it is the external photons that provide the main target for photopion production.

During flares, the proton synchrotron model predicts a higher-energy flux of neutrinos, but since the spectrum is harder and narrower than in the leptohadronic case, the corresponding total number of neutrinos is in fact lower. This will reflect on the predicted number of IceCube events, as discussed in the next section.

3.2. Expected Neutrino Event Rates

In this section, we estimate the number of expected neutrinos using the tabulated effective area for the point-source analysis with IceCube in its 86-string configuration and event selection applied in 2012[4] (Aartsen et al. 2017). To emulate the conditions of the realtime stream (Aartsen et al. 2017; Blaufuss et al. 2020) we apply an energy threshold of >100 TeV to the point-source effective area. At high energies the effective areas of the streams should converge.[5] The number of events is obtained by assuming the duration of the three different states mentioned above. We account for the fact that the detector operated with only a partial volume from 2008 August to 2011 May, by scaling the IC86 effective area with the square root of the ratio of deployed strings[6] (i.e., $\sqrt{40/86}$ during the phase of operation with the 40-string configuration, IC40).

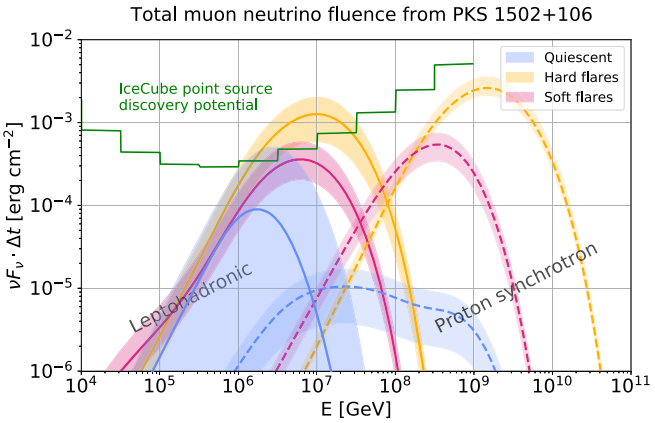

Figure 4. Total muon neutrino fluence from PKS 1502+106 predicted by the leptohadronic (solid) and protons synchrotron model (dashed) in the total duration of each of the three activity states. The curves correspond to the neutrino spectra of Figure 2, but the flux has now been integrated over the total duration of each activity state (3.8 yr quiescent, 3.7 yr of hard flares, and 3.5 yr of soft flares, see Table1). In green we represent the IceCube discovery potential of the seven-year point-source analysis for a decl. of 0° (Aartsen et al. 2017), where the flux has been integrated over the entire seven years of that analysis. We note that the discovery potential represented here should not be used for calculating precise model predictions, since the detector was still in construction during the investigated periods and the source is at 10° decl. Both these aspects were considered in obtaining the numbers shown in the bottom row of Table 2.

First, in order to compare the total neutrino fluence during the different activity states of the source we need to integrate the neutrino fluxes given in Figure 2 in the total duration of each state. The result is shown in Figure 4. For comparison, we show in green the differential fluence corresponding to the IceCube discovery potential at 0° (Aartsen et al. 2017). This has been obtained by multiplying the discovery potential flux of the seven-year point-source analysis with the duration of the experiment.

As we can see, during the entire course of the quiescent state, the source emits a total neutrino fluence of up to 10^{-3} erg cm^{-2} in the leptohadronic model (blue shaded area) on the left-hand side. It can therefore surpass the fluence corresponding to the IceCube point-source discovery potential; however, the best-fit (solid blue curve) yields only 2×10^{-4} erg cm^{-2}.

[4] https://icecube.wisc.edu/science/data/PS-3years

[5] We have used the published point-source effective area of IC86 instead of using the realtime effective area or the published effective areas of the partial detector configurations, because the IC86 effective area is available with a fine decl. binning of 0.01 in cosine decl., while the others distinguish only between up and down-going.

[6] We expect that vertical tracks scale with the ratio of the number of strings, while horizontal tracks would scale with the square root of the number of strings. Since we are mostly interested in high-energy events, the horizontal events are most relevant.

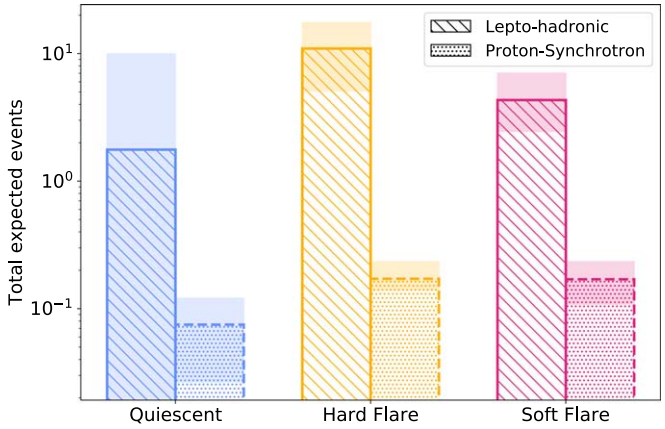

Figure 5. Total time-integrated number of IceCube events from PKS 1502+106, expected from the leptohadronic and protons synchrotron models, in the IceCube point-source analysis, in the entire duration of each of the three states indicated in Figure 1.

The neutrino fluence from hard flares in the leptohadronic model (solid yellow curve) surpasses the discovery potential even when its lower limit is considered. While the proton synchrotron model predicts a higher neutrino flux during hard flares (dashed yellow curve), the high neutrino energies place it below the discovery threshold due to absorption in the Earth, which makes the model more compatible with the lack of IceCube neutrino events during flares. The leptohadronic model is in tension with the lack of neutrino events during the hard flaring periods. On the other hand, as mentioned above, a considerable fraction of the hard flares of PKS 1502+106 took place during the construction phase of IceCube, when it was operating at partial effective volume, which lowers the overall average effective area. Furthermore, the green curve corresponds to the discover potential for a decl. of 0°, as published by the IceCube collaboration (Aartsen et al. 2014), while at the decl. of PKS 1502+106 (10°) the neutrino absorption in the Earth is higher, thus raising further the effective discovery potential fluence. Both these aspects are taken into account in the calculation of the predicted number of events below.

In Figure 5 we show the total number of events in IceCube predicted during the 11 yr period of Fermi-LAT observations from PKS 1502+106, separated into the three different activity states.

As we can see, the leptohadronic model predicts a larger number of neutrino events in all cases compared to proton synchrotron. In the quiescent state, that is due to a much higher emitted neutrino flux predicted by the model. During flaring states, the leptohadronic model predicts a broader and softer spectrum that also translates into a higher number of neutrinos. Moreover, the effective area drops with energy above 10 PeV due to absorption in the Earth, further reducing the number of observed events predicted by the proton synchrotron model.

The range of proton-injection luminosities shown as bands in Figure 2 translates into a systematic uncertainty in the number of IceCube events, shown as shaded regions in Figure 5. In the leptohadronic model, the number of events during the quiescent state ranges from zero to a few, while in the proton synchrotron model the value lies below 0.13. The most striking difference is in the number of events during the 3.8 yr of hard flares, which is 10.8 in the leptohadronic model, and only 0.17 in the proton synchrotron model. As discussed in the next section, these value ranges can be interpreted statistically, given the fact that no events were observed during flares, and one candidate neutrino from the source was observed during the quiescent state.

4. Discussion and Interpretation

Both leptohadronic and proton synchrotron models can explain the high-energy emission from PKS 1502+106 during the different epochs. This poses a challenge to distinguish between the two approaches. Moreover, the neutrino flux scales with the X-rays in both models, which are coproduced due to in-source cascades.

One distinction between the two models is the fact that while the leptohadronic model predicts the gamma-ray emission region to lie just outside the BLR ($R_{\rm diss} = (1.3\text{–}1.6) \times 10^{17}$ cm), in the proton synchrotron model that region lies further away ($R_{\rm diss} \geqslant 2.5 \times 10^{17}$ cm, see Table 2). While current observations cannot distinguish between these two scenarios, Fermi-LAT observations of the source place an upper limit on the dissipation radius of $R_{\rm diss} < 3 \times 10^{16-17}$ cm (Abdo et al. 2010; Karamanavis et al. 2016). Neither model can therefore be excluded based on current data. On the other hand, Ding et al. (2019) have constrained the dissipation radius of some short gamma-ray flares to as little as 3×10^{16} cm, based on a long period of observations of the source from 2014 to 2018. This indicates that some hadronic emission may also originate inside the volume of the BLR.

An interesting aspect of the leptohadronic model is its similarity to that applied to the 2014/15 neutrino flare of blazar TXS 0506+056 by Rodrigues et al. (2019) (see also the models by Reimer et al. 2019; Petropoulou et al. 2020). There, the presence of external fields from a BLR leads to a high flux of MeV photons and a low-energy cutoff in the gamma-ray spectrum. In terms of the origin of the multiwavelength fluxes, this model is also close to the interpretation by Gao et al. (2018) of the 2017 neutrino observed from TXS 0506+056: the soft X-rays (and potentially, hard gamma-rays) are interpreted as hadronic contributions, while the optical, hard X-rays, and soft gamma-rays are leptonic in origin. The difference is that in that case no external fields were considered. Keivani et al. (2018) have also provided a description of the multiwavelength emission from that source during the 2017 event that did include external fields, although in that case the hadronic component was subdominant even in X-rays.

Regarding energetics, one aspect that is shared by both models is the particularly high minimum Lorentz factors of the accelerated protons, $\gamma_p'^{\rm min}$. The high $\gamma_p'^{\rm min}$ is necessary to comply with the X-ray constraints, in contrast to the frequently used assumptions on the particle acceleration mechanisms. Therefore, specific assumptions would be necessary for the acceleration zone, for example, assuming only protons on the high-energy end of the spectrum can leak from the acceleration zone into the radiation zone (Katz et al. 2010). This assumption can be recently found in modern interpretations of ultrahigh-energy cosmic rays, as it can be shown that hard cosmic-ray escape spectra from the sources are needed to describe data for sources tracing the star formation rate, see e.g., Heinze et al. (2019); a detailed discussion of such escape mechanisms potentially producing such spectra can be found in Section IIIB of Zhang et al. (2018). Similar conditions may apply to the acceleration zone here.

Another criterion regarding energetics is the capability of the source to power the spectrum of nonthermal protons required by each model. To roughly estimate the plausibility of this energetic demand, the power required in protons can be compared to the Eddington luminosity of the source, which corresponds to the maximum power that can be steadily emitted by a black hole of a given mass. The Eddington luminosity of PKS 1502+106 can be estimated to be $L_{\rm Edd} = 10^{47}(M_{\rm BH}/10^9 M_\odot)$erg s^{-1}, where $M_{\rm BH} \approx 10^9 M_\odot$ is the black hole mass (D'Elia et al. 2003; Shen et al. 2011). At the same time, both models require a proton luminosity in the rest frame of the jet of $L'_{\rm p} = 5 \times 10^{44}$–$10^{46}$ erg s^{-1}. The corresponding physical luminosity (in the jet frame of the supermassive black hole) is $L_p^{\rm phys} = L'_p \Gamma_{\rm b}^2/2$. Given that the Lorentz factors predicted by the model are in the range of $\Gamma_{\rm b} = 30$–50, this yields a physical luminosity in protons in the range of 2–20 $L_{\rm Edd}$ for all the models. This figure is not significantly reduced during the quiescent state compared to the flares, if the best-fit parameters in Table 2 are considered. Although the Eddington luminosity does not set a hard limit on the available proton power, we can probably disfavor scenarios where the source must accelerate protons in a super-Eddington regime during long quiescent states. This energetic "crisis" of proton synchrotron blazars has already been noted by Liodakis & Petropoulou (2020), who studied a large sample of blazars including PKS 1502+106.

The latter observation certainly argues in favor of the leptohadronic model, where the quiescent state is compatible with an electron-only or electron-dominated emission. The quiescent states of the source would then be mostly dominated by the leptonic emission (for example between 2010 and 2015, see Figure 1). Sporadically, a neutrino-efficient state can be achieved through a temporary increase in the proton-injection power, with all other parameters unaltered, without significant changes in the UV, X-ray, or gamma-ray fluxes (blue shaded area in Figure 2, left-hand plot).

Regarding the number of IceCube events, we concluded that the proton synchrotron model predicts only between 0.03 and 0.17 neutrinos for each activity state. This would be consistent with seeing one neutrino from the source during the flaring state, if we assume that this is not the only source of this type in the Universe (i.e., by accounting for the Eddington bias, as discussed by Strotjohann et al. 2019). However, the argument can also be made that the emission of blazars can often be well described by a leptonic model, while in this work we describe the flares of PKS 1502+106 with a nonnegligible hadronic contribution. This would place the source in a "special" subclass of neutrino-efficient blazars that may be considerably more reduced compared to the total blazar population. Such an argument would then lead to a weaker effect of the Eddington bias.

In the case of the leptohadronic model the neutrino predictions are considerably higher, $1.77^{+8.23}_{-1.77}$ events predicted during the quiescent state (see Figure 5 and Table 2). This number is in agreement with the observation of one event by IceCube. On the other hand, the model also predicts a high number of events during flaring states, especially hard flares. In total $10.94^{-5.84}_{+6.56}$ events are expected, of which $7.97^{-4.25}_{+4.78}$ in the IC86 period, while either the IceCube realtime system was operational (starting from 2016, Aartsen et al. 2017) or an archival search was applied (Aartsen et al. 2018a). This means that our model predicts a minimum of $7.97–4.25 = 3.72$ high-energy events detected in IceCube during hard flares, which is in mild tension with the nondetection of any events (p-value of 2.4%, assuming Poisson statistics). We therefore strongly encourage a similar search for high-energy events during the flaring period in 2009: if also during that period no high-energy neutrino is found, the leptohadronic model would be disfavored much more significantly, with a p-value of $6 \cdot 10^{-3}$.

Finally, we note that Aartsen et al. (2020) have set a stringent 90% C.L. neutrino flux upper limit on PKS 1502+106 of $2.6 \times 10^{-13}(E_\nu/\text{TeV})^{-2}$ TeV^{-1} cm^{-2} s^{-1}. However, this limit was set assuming a power-law spectrum over a broad energy range, which is very different from the predicted spectral shapes by our models and can therefore not be directly compared to our results.

5. Summary and Conclusions

We have interpreted the multi-epoch, multiwavelength observations of PKS 1502+106, one of the brightest gamma-ray blazars detected. Using one-zone radiation models we have estimated the possible range of neutrino spectra emitted by the source while selfconsistently explaining the multiwavelength emission during its different states of electromagnetic activity: the quiescent state, and flares with a hard and with a soft gamma-ray spectrum. We have focused on the emission in the range from UV to gamma-rays, in their different flux levels over the 11 yr of Fermi-LAT observations. We have found that the emission can be well described with a hadronic contribution, both during quiescent and flaring states. In addition to best-fit results, we also provided an uncertainty range in the luminosity of nonthermal protons, which results in a systematic uncertainty in the neutrino emission level.

The X-ray fluxes observed during flares, which are typically bright and with a soft spectrum, are difficult to explain by means of a purely leptonic one-zone model. In both these models, this X-ray emission is a subdominant contribution originating in electromagnetic cascades initiated by hadronic interactions in the source. This point seems to support proton acceleration in PKS 1502+106 independently of neutrino emission.

Regarding the gamma-ray emission, in the lephohadronic model, it is most often dominated by inverse Compton scattering of photons from a broad line region. In the proton synchroton model, gamma-rays below 1 GeV originate in the proton synchrotron emission, and those above 1 GeV originate from electron/positron pairs produced by those same protons. On the other hand, the archival radio observations from the source cannot originate in a region as compact as the one modeled in this work, because of its radio-opacity due to synchrotron self-absorption. This suggests a larger dissipation region in the jet with efficient electron synchrotron emission. It is noteworthy that the bright radio emission from the source in the years leading up to the neutrino emission seems to point toward a correlation (or possibly even a common origin) between radio and neutrino emission. This point is driven further by statistical correlations found between radio-loud AGN and the observed high-energy neutrinos (Hovatta et al. 2020; Plavin et al. 2020). However, our extensive scan of the source's parameter space has revealed that such common origin is not feasible within a one-zone model, and other more complex geometries may be necessary to potentially establish such a bridge.

We have then drawn conclusions on the viability of the two models based on energetics and their predictions for the neutrino flux. The main difference between the two models is that the proton synchrotron model requires constant acceleration of protons, even during the quiescent state, in order to explain X-ray and gamma-ray observations. This implies a constant neutrino output from the source, which is statistically below the IceCube sensitivity. At the same time, the model demands a super-Eddington power in nonthermal protons during the entire quiescent state, which presents a major challenge from the energetic point of view.

On the other hand, a leptohadronic model is compatible with a purely leptonic solution during quiescent states. This suggests a quiescent state that is dominated by the electron emission most of the time, but is also compatible with periods of efficient neutrino emission through temporary increases in the injection of nonthermal protons without significant changes in the multiwavelength emission. This can help explain the IceCube event 190730A from the direction compatible with the position of the source. Moreover, similar models have been used in the literature to explain the multiwavelength emission from blazar TXS 0506+056 during the 2017 neutrino event. The limitation of the leptohadronic model resides in the high number of IceCube events ($7.97^{-4.25}_{+4.78}$) predicted during hard gamma-ray flares since the beginning of the realtime alert system. This result is in mild tension with the nonobservation of neutrino events during flares. An archival search of IceCube events from the direction of the source before 2010 could help constrain more significantly this leptohadronic model: if no events were found, the model would be excluded with a p-value of $6 \cdot 10^{-3}$.

We would like to thank Robert Stein and Anatoli Fedynitch for fruitful discussions, Julia Tjus for comments on the manuscript, and Foteini Oikonomou for pointing out an inconsistency in an early version of the manuscript. This work has been supported by the Initiative and Networking Fund of the Helmholtz Association and by the European Research Council (ERC) under the European Unions Horizon 2020 research and innovation program (grant No. 646623).

ORCID iDs

Xavier Rodrigues https://orcid.org/0000-0001-9001-3937
Simone Garrappa https://orcid.org/0000-0003-2403-4582
Shan Gao https://orcid.org/0000-0002-5309-2194
Vaidehi S. Paliya https://orcid.org/0000-0001-7774-5308
Anna Franckowiak https://orcid.org/0000-0002-5605-2219
Walter Winter https://orcid.org/0000-0001-7062-0289

References

Aartsen, M., Ackermann, M., Adams, J., et al. 2018a, Sci, 361, 1378
Aartsen, M., Ackermann, M., Adams, J., et al. 2018b, Sci, 361, 147
Aartsen, M., Ackermann, M., Adams, J., et al. 2020, PhRvL, 124, 051103
Aartsen, M. G., Abbasi, R., Abdouand, Y., et al. 2013, Sci, 342, 1242856
Aartsen, M. G., Abraham, K., Ackermann, M., et al. 2017, ApJ, 835, 151
Aartsen, M. G., Ackermann, M., Adams, J., et al. 2014, ApJ, 796, 109
Aartsen, M. G., Ackermann, M., Adams, J., et al. 2017, APh, 92, 30
Abdo, A. A., Ackermann, M., Ajello, M., et al. 2010, ApJ, 710, 810
Ajello, M., Angioni, R., Axelsson, M., et al. 2019, ApJ, 892, 105
An, T., Hong, X. Y., Venturi, T., Jiang, D. R., & Wang, W. H. 2004, A&A, 421, 839
Atoyan, A., & Dermer, C. D. 2001, PhRvL, 87, 221102
Becker, J. K. 2008, PhR, 458, 173
Becker Tjus, J., Eichmann, B., Halzen, F., Kheirandish, A., & Saba, S. M. 2014, PhRvD, 89, 123005
Blaufuss, E., Kintscher, T., Lu, L., & Tung, C. F. 2020, PoS, ICRC2019, 1021
Cerruti, M., Zech, A., Boisson, C., et al. 2019, MNRAS, 483, L12
Crowther, J. H., & Clarke, R. W. 1966, MNRAS, 132, 405
D'Elia, V., Padovani, P., & Landt, H. 2003, MNRAS, 339, 1081
Diltz, C., Boettcher, M., & Fossati, G. 2015, ApJ, 802, 133
Dimitrakoudis, S., Mastichiadis, A., Protheroe, R. J., & Reimer, A. 2012, A&A, 546, A120
Ding, N., Gu, Q. S., Geng, X. F., et al. 2019, ApJ, 881, 125
Francis, P. J., Hewett, P. C., Foltz, C. B., et al. 1991, ApJ, 373, 465
Franckowiak, A., Garrappa, S., Paliya, V., et al. 2020, ApJ, 893, 162
Gallo Rosso, A., Mascaretti, C., Palladino, A., & Vissani, F. 2018, EPJA, 133, 267
Gao, S., Fedynitch, A., Winter, W., & Pohl, M. 2018, NatAs, 3, 88
Gao, S., Pohl, M., & Winter, W. 2017, ApJ, 843, 109
Garrappa, S., Buson, S., Franckowiak, A., et al. 2019, ApJ, 880, 103
Ghisellini, G., & Tavecchio, F. 2009, MNRAS, 397, 985
Giommi, P., Glauch, T., Padovani, P., et al. 2020, MNRAS, 497, 865
Greene, J. E., & Ho, L. C. 2005, ApJ, 630, 122
Hartman, R. C., Bertsch, D. L., Bloom, S. D., et al. 1999, ApJS, 123, 79
Heinze, J., Fedynitch, A., Boncioli, D., & Winter, W. 2019, ApJ, 873, 88
Hewett, P. C., & Wild, V. 2010, MNRAS, 405, 2302
Hovatta, T., Lindfors, E., Kiehlmann, S., et al. 2020, arXiv:2009.10523
Kadler, M., Krauß, F., Mannheim, K., et al. 2016, NatPh, 12, 807
Karamanavis, V., Fuhrmann, L., Krichbaum, T. P., et al. 2016, A&A, 586, A60
Katz, B., Meszaros, P., & Waxman, E. 2010, JCAP, 10, 012
Keivani, A., Murase, K., Petropoulou, M., et al. 2018, ApJ, 864, 84
Kiehlmann, S., Hovatta, T., Kadler, M., Max-Moerbeck, W., & Readhead, A. C. S. 2019, ATel, 12996
Krauß, F., Deoskar, K., Baxter, C., et al. 2018, A&A, 620, A174
Liodakis, I., & Petropoulou, M. 2020, ApJL, 893, L20
Mannheim, K. 1993, A&A, 269, 67
Mannheim, K. 1995, APh, 3, 295
Mannheim, K., Stanev, T., & Biermann, P. L. 1992, A&A, 260, L1
Mastichiadis, A. 1996, SSRv, 75, 317
Meyer, M., Scargle, J. D., & Blandford, R. D. 2019, ApJ, 877, 39
Morton, T., Drake, A. J., Djorgovski, S. G., et al. 2008, ATel, 1661, 1
Murase, K. 2017, in Neutrino Astronomy: Current Status, Future Prospects, ed. T. Gaisser & A. Karle (Singapore: World Scientific)
Oikonomou, F., Murase, K., Padovani, P., Resconi, E., & Mészáros, P. 2019, MNRAS, 489, 4347
Paliya, V. S., Marcotulli, L., Ajello, M., et al. 2017, ApJ, 851, 33
Petropoulou, M., Murase, K., Santander, M., et al. 2020, ApJ, 891, 115
Pian, E., Ubertini, P., Bazzano, A., et al. 2011, A&A, 526, A125
Plavin, A. V. c., Kovalev, Y. Y., Kovalev, Y. A., & Troitsky, S. V. 2020, ApJ, 894, 101
Protheroe, R. J. 1999, NuPhS, 77, 465
Reimer, A., Boettcher, M., & Buson, S. 2019, ApJ, 881, 46
Rodrigues, X., Gao, S., Fedynitch, A., Palladino, A., & Winter, W. 2019, ApJL, 874, L29
Scargle, J. D., Norris, J. P., Jackson, B., & Chiang, J. 2013, ApJ, 764, 167
Shao, X., Jiang, Y., & Chen, X. 2019, ApJ, 884, 15
Shen, Y., Richards, G. T., Strauss, M. A., et al. 2011, ApJS, 194, 45
Stecker, F. W., Done, C., Salamon, M. H., & Sommers, P. 1991, PhRvL, 66, 2697
Strotjohann, N. L., Kowalski, M., & Franckowiak, A. 2019, A&A, 622, L9
Szabo, A. P., & Protheroe, R. J. 1994, APh, 2, 375
Vitagliano, E., Tamborra, I., & Raffelt, G. 2020, RcMP, 92, 045006
Zhang, B. T., Murase, K., Kimura, S. S., Horiuchi, S., & Mészáros, P. 2018, PhRvD, 97, 083010